International Journal of Computer Information Systems and Industrial Management Applications
ISSN 2150-7988 Volume 18(19s) 2026 pp. 334-254
https://doi.org/10.70917/ijcisim-2026-5022
Article

Design and Characterization of a Fiber Bragg Grating-Based Sensor System for Multi-Parameter and Real-Time Monitoring

Amit Kumar Sawasakade*[1], Dr. Anubhuti Khare[2]

*[1]Research Scholar, Dept. of Electronics and Communication Engineering, RGPV, Bhopal, India
[2]Guide & Professor, Dept. of Electronics and Communication Engineering, RGPV, Bhopal, India
Corresponding author: amitsawasakade26@gmail.com

Abstract: Fiber Bragg grating (FBG) sensors are dielectric, chemically inert, immune to electromagnetic interference and intrinsically multiplexable but their application in multi-parameter monitoring is limited by the cross-sensitivity: one reflected peak cannot distinguish a temperature change from a strain change. In this paper, a four-element, wavelength-division-multiplexed FBG sensor system is designed and characterized which can measure, simultaneously and in real-time, the temperature and the axial strain from a single fiber, in addition to the thermal field at four points along an eight metre span. The architecture is modeled in OptiSystem 21: a broadband source, a three-port circulator, the bidirectional fiber span and four uniform gratings, positioned on a 2 nm grid at 4 different wavelengths of 1546, 1548, 1550 and 1552 nm. The reflected spectrum is then processed in a MATLAB co-simulation component that implements a thresholded centroid peak estimation and an inversion of a sensitivity matrix. The reflectivity of the modelled resonance is 59 % and the full width at half maximum is approximately 0.13 nm, which is 10 times narrower than the channel spacing. Single-parameter sweeps provide a coefficient of determination > 0.999 with a sensitivity of 10.0 pm/°C between 0 and 100 °C and 1.2 pm/με between 0 and 1000 με. A 2×2 sensitivity matrix with a determinant of −11 pm2/°C•με and a full scale scaled condition number of 2.78 is obtained by a grating pair that is differentially packaged, with a strain sensitivity difference greater than an order of magnitude (1.2 pm/με versus 0.1 pm/με) and whose thermal sensitivities are matched. The inversion is applied simultaneously at seven distinct values of temperature and strain to reproduce the applied values of these measurands with an accuracy of 3×10^{-14} °C and 1.2×10^{-13} με, which is limited by the arithmetic used and is independent of the accuracy of the method. Under noise, the centroid estimator finds the resonance at 1550 nm at 1549.9999 nm, and the demodulation error over a 1000 pm span is ±1.08 pm, which corresponds to 0.12 °C and 1.39 με after inversion. Repeatability after five thermal cycles is 0.40 pm, thermal linearity is $R^2 = 0.9998$, the hysteresis is 92.69 pm (full loop 0–100 °C) and the first order time constant of the interrogation chain is 100 ms sampled at 20 Hz.

Keywords: Fiber Bragg grating; OptiSystem simulation; multi-parameter sensing; temperature–strain discrimination; cross-sensitivity decoupling; sensitivity matrix inversion; wavelength-division multiplexing; centroid peak detection; real-time interrogation

1. Introduction

The increasing instrumentation of safety-critical assets, such as civil structures, aerospace composites, electrochemical energy storage and process plant, require simultaneous monitoring of multiple physical fields at the same point in space. This requirement is met with conventional electrical transducers only by the co-location of dissimilar devices accompanied by their own lead-out wiring, excitation circuitry and susceptibility to electromagnetic interference. The cable burden, as a result of the conditions imposed on the cable, is often the primary source of failure in the monitoring system itself and the cost of installing it.

Structurally elegant alternative is fiber Bragg gratings. A grating is a periodic modulation of the core refractive index, which results in back-reflection of a narrow spectral band around the Bragg wavelength, which means that the encoding of the measurand in the wavelength, rather than the intensity, makes the device self-referencing and means that it is not affected by source fluctuation and connector loss. A grating only takes up a few millimetres of an otherwise unremarkable telecommunications fiber, so that a number of sensing points can be addressed serially along a single dielectric lead. These characteristics have facilitated the ongoing development of FBG instrumentation in diverse fields such as structural health monitoring, battery diagnostics, geotechnics and biomedical measurement [12], [15].

The Bragg resonance is also a phenomenon with the same property of being both robust and ambiguous. The wavelength shift combines the thermo-optic and thermal-expansion response of silica with the elasto-optic response to mechanical loading, so a single reflected peak is a scalar projection of a multi-dimensional measurand vector. If that projection is interpreted as one physical quantity, then there is a systematic error which depends linearly on the excursion of the confounding field; for the strains which were chosen in Section 6.2, a full-scale strain of 1000 με would displace the resonance by the same amount as a temperature excursion of 120 °C, so that an uncompensated strain gage would report the wrong temperature at greater than its full range. This cross-sensitivity is the main challenge to the implementation of FBG arrays in truly multiparameter service.

There are two complimentary approaches that have surfaced. The first type involves shaping the transducer to allow 2 or more spectral features to be sensitive to different ratios [2]–[6]—this can be done through dual-wavelength, dual-diameter gratings, tapered and etched fibers, tilted gratings and superstructure gratings, as well as hybrid architectures involving the combination of a grating with an interferometric cavity. The second one works on the interrogation record, utilizing matrix inversion, least-squares estimation or learned demodulation models which are able to resolve overlapping resonances that are not easily achievable by conventional peak-finding [1], [13]. Both strands have progressed significantly since 2020, but the majority of the reported systems are still "one-at-a-time" demonstrations, and few report the metrics of the estimator, such as noise-limited resolution, hysteresis, repeatability, and response time, that are required to determine whether the demonstrated discrimination will survive in service.

This present work attempts to overcome this deficiency with a full simulation study that has been carried out in OptiSystem 21 with a MATLAB co-simulation demodulator. A 4 element wavelength division multiplexed array is modelled, the temperature and axial strain discrimination is achieved not by a special inscription geometry but by the differential packaging of nominally identical gratings so that they have a sensitivity contrast with respect to the strains. The sensitivity matrix is filled independently for each field, the numerical conditioning of the matrix is measured, and the decoupling operator obtained is checked for simultaneous excursions of both fields. Then the process of interrogation is itself characterized, in its own right — peak-detecting with noise, error in demodulation, resolution as a function of optical signal-to-noise ratio, error in linear approximation, hysteresis, repeatability and dynamic response — based on the behaviour of the estimator, and the real-time claim is up for grabs on grounds of quantified behaviour, rather than on assertion. Lastly, the four gratings are exercised as a distributed thermal probe along an eight-metre fiber, revealing a spatial-sampling constraint, which no wavelength accuracy can fix.

2. Literature Review

Three major trends in the work done from 2020 to 2025 can be arranged in a triangular fashion, each with significant advances and a defining challenge: transducer architecture, coating chemistry and demodulation intelligence.

Her and Lin [3] were able to achieve the strain–temperature discrimination by bonding one half of the grating's length to a host structure and leaving the other half free, which is an elegant scheme, but requires a controlled adhesive boundary, which is not easily achievable in the field. Dey et al. [4] used the sensitivity contrast due to the chemical etching of the cladding, with the trade-off of a compromised fiber, however. Yang et al. [2] positioned two sub-gratings with respect to each other across a micrometric air gap, such that the phase-shifted grating and Fabry–Perot fringes appeared in the same reflection spectrum, with the free spectral range parameterized by the gap length. Zhao et al. [5] and Xiao et al. [6] followed different paths to achieve the interferometric sensitization (Vernier-effect cascade and peanut-taper Mach–Zehnder, respectively) with large sensitivity amplification, but with a periodic transfer function with limited range of unambiguous resolution. All of these devices have a processing step that is not needed by the average uniform grating: the common thread is that discrimination is bought with fabrication complexity.

To measure something other than thermal and mechanical fields, an FBG must thus be overlaid with a second transducing field, and the literature on such overlays is illustrative even when the additional measurand is not the main one of interest, since the overlay would always affect the thermal coefficient of the underlying grating. Polyimide is the standard material for relative humidity measurements, and Mihailov et al. [8] have demonstrated that the removal of the steps of stripping, hydrogen-loading and recoating by femtosecond writing through an undamaged polyimide jacket has reduced the need for these steps, improving the uniformity and hysteresis of relative humidity measurement. Peng et al. [7] then used a standard grating in combination with a porous anodic alumina interference film to measure both temperature and humidity, with the result being 10.4 pm/°C and 185 pm/%RH, respectively, which is another example of the difference of dynamic range of grating versus film features on a single instrument. Ma et al. [14] considered thin-film and Fabry–Perot type architectures more generally, and found several reliability limitations that appeared repeatedly in these types of architectures: adhesion of the coatings, ageing effects and thermal cross-talk. Compact assemblies for combined measurement of both temperature and pressure have been reported by Xu et al. [16] where the pressure response is controlled by the mechanical gain of the diaphragm instead of by the intrinsic response of silica.

The lithium-ion battery has emerged as a challenging test case because the temperature and strain change together in a chemically aggressive, enclosed battery. Huang et al. [11] demonstrated the ability of embedding gratings into a cell to recover, in real-time, the internal temperature, validated by a finite-element thermal model, and Unterkofler et al. [10] proved that a grating designed as a temperature probe should be mechanically isolated from the swelling of the electrodes; a principle that is followed in the present array with the use of a reference element. Li et al. [9] showed that it is possible to amplify the transferred strain using a hinged, differential-lever structure, thereby proving that, conversely, the strain coefficient can be deliberately enhanced.

Several groups have tried to loosen the requirement that adjacent gratings must occupy disjoint spectral windows, due to the fact that the multiplexing density is limited by the source bandwidth. Arockiyadoss et al. [1] used a transformer network with mixed-linewidth arrays, and achieved good results of recovering each Bragg wavelength even for strong spectral overlap. The other constraint, limited resolution in a low cost embedded acquisition application, has been tackled by Mao et al. [13] who presented a neighbourhood-averaging interrogation scheme, and Dwivedi et al. [12] who optimized apodization profiles for quasi-distributed monitoring, demonstrating that channel spacing is directly controlled by side-lobe suppression. Theodosiou [15] noted the trend of the field moving toward system-level integration instead of novelty in transducers. These contributions are summarized in Table 1, which groups them by the criteria pertinent to the current goal.

Table 1. Representative fiber Bragg grating multi-parameter sensing studies published between 2020 and 2025.

Ref. / Year	Sensing architecture	Para-meters	Discrimination mechanism	Real-time operation	Reported performance
[3] 2020	Half-bonded / half-free single FBG	2	Two-equation solution from bonded and free segments	Not reported	Verified against thermocouple and beam theory
[4] 2022	Cladding-etched silica FBG pair	2	Sensitivity contrast from differential cladding diameter	Not reported	Stable simultaneous strain–temperature recovery
[6] 2022	Peanut-taper Mach–Zehnder interferometer	2	Dual interference dips with distinct sensitivity ratios	Not reported	High sensitivity; restricted unambiguous range
[5] 2023	Vernier-effect cascaded fiber cavity	2	Envelope amplification of two cavity responses	Not reported	Large sensitivity magnification factor

Ref. / Year	Sensing architecture	Para-meters	Discrimination mechanism	Real-time operation	Reported performance
[7] 2023	FBG cascaded with porous anodic alumina film	2	Grating peak for temperature, film fringe for humidity	Not reported	10.4 pm/°C; 185 pm/%RH
[8] 2023	Through-the-coating femtosecond polyimide FBG	2	Coating swelling superimposed on thermal response	Not reported	Improved coating uniformity, reduced hysteresis
[2] 2024	Air-gap FBG combining PSFBG and FPI spectra	2	Two co-existing features in one reflection band	Not reported	Free spectral range tunable with gap length
[9] 2024	Hinged differential-lever sensitized FBG pair	2	Mechanical amplification plus thermal reference	Not reported	Enhanced strain sensitivity in overcharge tests
[11] 2024	FBG array embedded in Li-ion cell	1–2	Spatial separation of internal and external gratings	Demonstrated	Model–experiment agreement within about 5 %
[1] 2025	Mixed-linewidth network, transformer demodulator	1	Learned separation of overlapping spectra	Cloud, near real-time	Robust recovery under severe spectral overlap
This work	Four-element WDM array modelled in OptiSystem	2 fields at 4 points	Differential-packaging pair with 2×2 sensitivity-matrix inversion	τ = 100 ms, 20 Hz sampling	±1.08 pm demodulation error → 0.12 °C, 1.39 με

3. Research Gap Identification

The majority of reviewed literature concerns transducers which are characterized under one-at-a-time excitation with a constant (or fixed) confounding field rather than a variable one. It is therefore inappropriate to use the reported accuracies as limits on the error that occurs when both fields are moving simultaneously, the only case of practical interest. If a matrix or closed-form inversion is used, the numerical conditioning of the matrix is rarely quantified, and a reader may not be able to judge how the quoted wavelength uncertainty is propagated into the uncertainty of the measurand — and it is the numerical conditioning that governs the propagation of the uncertainty, not the sensitivity.

Another – not widely recognized – is the interrogation chain instead of the transducer. Though the studies of demodulation increase the levels of spectral separation, they typically do not go beyond the recovery of measurand but the demonstrations of application are made in real time, without the availability of a validated decoupling operator. The ability to detect peaks in noise, the resolution as a function of optical signal-to-noise ratio, the hysteresis through a full thermal cycle, and cycle-to-cycle repeatability, and the time constant of the measurement are rarely reported together for one system, and almost never in conjunction with the decoupling analysis to which they give constraints. If the estimates of the wavelength sent to the decoupling operator have only a ten-picometre level of uncertainty, the algebraically exact one is useless, but it is described in a different literature.

A third gap is related to the lack of spatial sampling. Multiplexed arrays are often said to be quasi-distributed but the correctness of the grating pitch in comparison with the spatial bandwidth of the measurand field is rarely discussed, and an array can report good internal consistency to miss the extremum it was installed to measure. No reported system provides simultaneously decoupled temperature and strain from a multiplexed array, conditions the inversion of this array, characterizes an estimator that feeds into this system across noise, hysteresis, repeatability and response time, and considers the limit of the spatial sampling of the same array.

4. Objectives of the Study

The investigation is structured around 4 objectives each corresponding to a specific simulation activity and body of evidence:

Objective 1. To design, in the OptiSystem environment, a 4 element wavelength-division-multiplexed FBG array with a wavelength interval of 2nm, for which a wavelength sensitivities coefficient is chosen according to the packaging, instead of a special grating geometry, to obtain selectivity with respect to the axial load and to verify that the spectral distance between the channels is larger than the maximum differential grating-drifting of the array due to the combined loading.

Objective 2. To characterize the array over the entire operating range via independent temperature and strain sweeps, to fill in the responses of the array and quantify the numerical conditioning of the 2×2 sensitivity matrix, and to determine the linearity, hysteresis and cycle-to-cycle repeatability of the thermal response.

Objective 3. To formulate, implement and validate an algorithm for matrix inversion decoupling under simultaneous temperature–strain excitations, and to isolate the error introduced by the algorithm for the algebra of the matrix inversion from the error introduced by the algorithm that supplies the input to the algebra, namely the wavelength estimator algorithm.

Objective 4. To measure the real time viability of the interrogation chain in terms of the accuracy in peak detection under noise, the demodulation error, its capability of resolution with the range of optical signal/noise ratio that a practical interrogator might operate in and its dynamic response, and to determine the spatial-sampling limit of the array as a distributed thermal probe.

5. Methodology

5.1 Governing relations

The period Λ of a uniform grating is inscribed in an effective index neff of the core and is the resonance λB

$=2\ neff\ \Lambda$. By differentiating with respect to the two fields of interest and keeping first order terms, the constitutive relation for the i'th element of the array is obtained,

$$\Delta\lambda i\ =\ KiT\ \Delta T\ +\ Ki\varepsilon\ \Delta\varepsilon \qquad \textbf{(1)}$$

in which the coefficients aggregate the underlying physics. The thermal coefficient combines the thermo-optic and thermal-expansion contributions, KiT = λB (ξ + αf), augmented for bonded elements by the differential expansion of the substrate. The mechanical coefficient follows from the effective photo-elastic constant, Kiε = λB (1 – pe) with pe ≈ 0.22 for germanosilicate fiber, but only in so far as the strain of the host is actually transferred to the fiber core: an element housed in a strain-isolating capillary retains its thermal coefficient while its mechanical coefficient collapses toward zero. That asymmetry — a coefficient that packaging can suppress beside one that packaging cannot — is the mechanism on which the present discrimination scheme rests. Collecting an element pair A and B yields

$$\Delta\lambda\ =\ K\ \bullet\ m,\ \ m\ =\ [\Delta T, \Delta\varepsilon]^{\mathrm{T}},\ \ K\ =\ \big[[KAT, KA\varepsilon], [KBT, KB\varepsilon]\big] \qquad \textbf{(2)}$$

So that recovery reduces to the inversion m = K⁻¹ Δλ, which is well posed provided the rows of K are sufficiently linearly independent. With matched thermal coefficients the determinant reduces to det K = KAT (KBε – KAε), so the conditioning of the problem is governed entirely by the contrast between the two strain coefficients and is degraded, not improved, by any packaging change that allows strain to leak into the reference element. Because the two measurands carry dissimilar units, conditioning is assessed on the dimensionless matrix obtained by scaling each column by its full-scale span, every entry then expressing a full-scale wavelength contribution in picometres.

5.2 OptiSystem model construction

The complete sensing system was implemented in OptiSystem 21. Broadband illumination is launched through a three-port optical circulator into a bidirectional optical fiber span representing the lead-in cable, at the far end of which the instrumented section carries four uniform fiber Bragg grating components configured in the bidirectional mode required for reflection-port analysis. The gratings are placed on a regular 2 nm grid at 1546, 1548, 1550 and 1552 nm and are distributed along the sensing fiber at 0, 2, 4 and 6 m, so that the same array serves both as two temperature–strain discrimination pairs and as a four-point thermal profiler. The reflected field returns through port three of the circulator to an optical spectrum analyser, a photodetector and an oscilloscope for time-domain observation, and is passed to a MATLAB component that executes the peak-estimation and decoupling routines. Figure 1 shows the project layout, in which the nested parameter-sweep configuration spanning 20–100 °C and 0–1000 με is also visible, and Table 2 lists the grating component parameters.

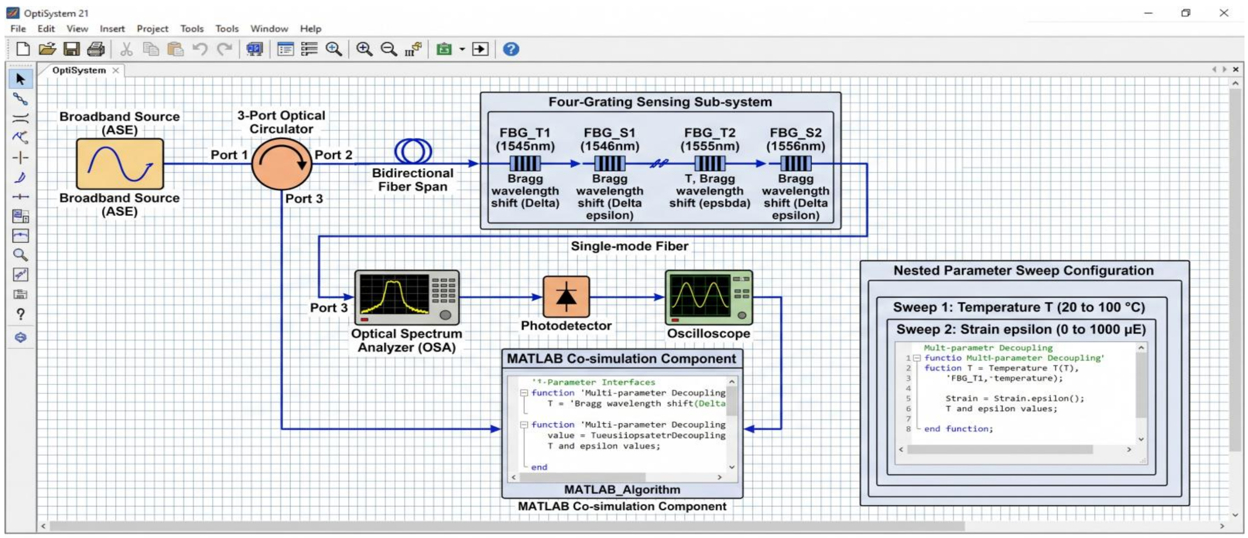

Figure 1. OptiSystem 21 project layout of the proposed multi-parameter FBG sensor system, showing the broadband source, circulator, bidirectional fiber span, four-grating sensing sub-system, visualizers, MATLAB co-simulation component and the nested parameter-sweep configuration.

Figure 1. OptiSystem 21 project layout of the proposed multi-parameter FBG sensor system, showing the broadband source, circulator, bidirectional fiber span, four-grating sensing sub-system, visualizers, MATLAB co-simulation component and the nested parameter-sweep configuration.

Table 2. Uniform fiber Bragg grating component parameters configured in OptiSystem.

Parameter	FBG_1	FBG_2	FBG_3	FBG_4	Remarks
Bragg wavelength (nm)	1546.00	1548.00	1550.00	1552.00	Regular 2 nm channel grid
Sensing role	Strain-coupled (A)	Strain-isolated (B)	Strain-coupled (A)	Strain-isolated (B)	Two discrimination pairs
Position along sensing fiber (m)	0	2	4	6	Multi-point thermal profiling
Grating length (mm)	13	13	13	13	Component ‘Length’ parameter
Index modulation Δn	4.9×10^{-5}	4.9×10^{-5}	4.9×10^{-5}	4.9×10^{-5}	Sets reflectivity via $\tanh^2(\kappa L)$
Effective index	1.447	1.447	1.447	1.447	Standard SMF-28 core

Apodization	Uniform	Uniform	Uniform	Uniform	Identical inscription for all elements
Peak reflectivity (%)	59	59	59	59	Read from the modelled spectrum
FWHM bandwidth (nm)	0.13	0.13	0.13	0.13	≈ 6.5 % of the channel spacing
Thermal sensitivity KT (pm/°C)	10.0	10.0	10.0	10.0	Matched across the array by design
Strain sensitivity Kε (pm/με)	1.2	0.1	1.2	0.1	Contrast created by packaging alone
Assumed packaging	Epoxy bond to host	Strain-isolating capillary	Epoxy bond to host	Strain-isolating capillary	Determines the strain coefficient
Operating span	0–100 °C / 0–1000 με	0–100 °C / 0–1000 με	0–100 °C / 0–1000 με	0–100 °C / 0–1000 με	Full-scale spans used for scaling K
Segments / calculation	100, coupled-mode	100, coupled-mode	100, coupled-mode	100, coupled-mode	Transfer-matrix solution per segment

5.3 Simulation parameters and sweep strategy

Global parameters were chosen to ensure that the energy sampling of the spectral grid ensures that each Bragg peak is sampled with an appropriate margin and to ensure that the sweep campaigns test all the claims presented in Section 6. The four channels are included in the modelled window (1544–1554 nm) and the 0.13 nm resonance width is covered by numerous points, resulting in a well-resolved line shape being used by the centroid estimator, rather than a few points. The detuning effect for each grating was applied by an iterative nested parameter sweep on the Bragg frequency of the grating, and the detuning offset was calculated from equation (1) with packaging-dependent coefficients provided in Table 2.

Five campaigns were carried out. The temperature was swept from 0° to 100 °C in steps of 10 °C at zero strain, which filled one column of the sensitivity matrix, while the strain was swept from 0 to 1000 με in increments of 100 με at a constant temperature, which filled the other column of the sensitivity matrix. A total of 7 combined operating points were subsequently set at which both fields varied at the same time from the reference values and covered the range of 20 – 80 °C and 100 – 700 με. A hysteresis campaign was executed, taking the entire 0 to 100 to 0 °C loop twice, first ascending and then descending, while a repeatability campaign was conducted five times from ambient to 50 °C. Finally, the OSNR was varied from 40 dB to 75 dB to obtain the noise limited OSNR and a dynamic record of sixty seconds was taken with a sampling rate of 20Hz to characterize the time response. The configuration is recorded in Table 3 below.

Table 3. Global simulation parameters and component configuration in OptiSystem 21.

Setting	Value	Rationale
Reference wavelength	1550 nm	Centres the modelled spectral window

Channel plan	1546 / 1548 / 1550 / 1552 nm	Regular 2 nm grid, four channels
Modelled spectral window	1544–1554 nm	Covers the array plus full-scale detuning
Source	Broadband ASE source	Uniform illumination of all four channels
Circulator	Three-port	Separates launch and reflection paths
Fiber span	Bidirectional single-mode lead-in plus 8 m instrumented section	Represents the cable and the sensing region
Grating positions	0, 2, 4 and 6 m	Gives a 2 m spatial sampling pitch
Temperature sweep	0–100 °C in 10 °C steps	Populates the thermal column of K
Strain sweep	0–1000 με in 100 με steps	Populates the mechanical column of K
Combined validation points	7 points, 20–80 °C and 100–700 με	Tests the inversion under joint excitation
Hysteresis campaign	0 → 100 → 0 °C, branches recorded separately	Quantifies loop separation
Repeatability campaign	5 return cycles to 50 °C	Quantifies cycle-to-cycle scatter
OSNR sweep	40–75 dB	Sets the wavelength-estimation noise floor
Dynamic record	60 s at 20 Hz sampling	Characterizes the time response
Peak estimation	Centroid over samples above 30 % of peak reflectivity	Sub-resolution localization of each channel
Co-simulation	MATLAB component executing peak estimation and K^{-1}	Recovers the measurand vector per frame

5.4 Peak estimation and decoupling routine

In the MATLAB block the sampled reflection spectrum is first divided into four windows defined by the nominal channel boundaries. The intensity-weighted centroid of the samples that are above 30 % of the local peak reflectivity is used as an estimate of the Bragg wavelength within each window. The threshold is used for two reasons: firstly to suppress the noise floor contribution to the weighted sum and secondly to ensure that the estimated resonance line centre is close to the near-symmetric central portion of the resonance where the centroid is an unbiased estimator of the line centre. The variance for the centroid is significantly lower than the sample spacing, because it is an average over all samples in the accepted region, not just the largest one, as is the case for the sample spacing, which is how the sub-picometre localization in Section 6.8 is possible.

The observation vector in the equation (2) is the refined wavelengths of the two elements of a discrimination pair, which are pre-computing multiplied by the inverse matrix. The operator K^{-1} is calculated offline using LU decomposition with partial pivoting and checked using the singular-value decomposition. Conditioning is defined by the spectral condition number of the full-scale-scaled matrix; if the condition number is near unity (1) then the responses of the two elements are mutually orthogonal, while a value of order 10^3 would imply that the two elements respond nearly in proportion, and that noise is amplified catastrophically during inversion.

6. Results and Discussion

6.1 Spectral design and channel separability

The design of the array is shown in figure 2. The reflection spectrum of a single grating as part of the reference condition is shown in panel (a): The resonance is centered at 1550.0 nm, the peak reflectivity is 59 % and the full width at half maximum is approximately 0.13 nm, with an out-of-band floor that cannot be resolved from zero with the linear scale. The composite spectrum of the four-element array is shown in panel (b) where the channels at 1546, 1548, 1550 and 1552 nm are clearly separated and there is no measurable overlap between the adjacent line shapes.

The absolute excursion of a grating, as shown in the result surface of Figure 4(a), is 2.2 nm over the entire operating range, with 1000 pm due to thermal shift and 1200 pm due to mechanical shift, and this is above the channel spacing of 2 nm. However, collision in the channel is prevented, since it is the differential shift between the neighbor channels that are threatening the guard band. The thermal coefficients of the array are equal at 10.0 pm/°C, so that the temperature term does not contribute to the differential; only the difference in strain-coefficients, 1.1 pm/με, does so, resulting in a worst case differential detuning of 1.1 nm at maximum strain against the 2 nm spacing. The array still therefore has a 0.9 nm guard band under the most severe combination of fields, and the separability demanded by Objective 1 is achieved, not as a result of the spacing alone, but by deliberate matching of the thermal coefficients also. If the packaging had been given a chance to intrude upon the thermal match, the same spacing would not have been sufficient.

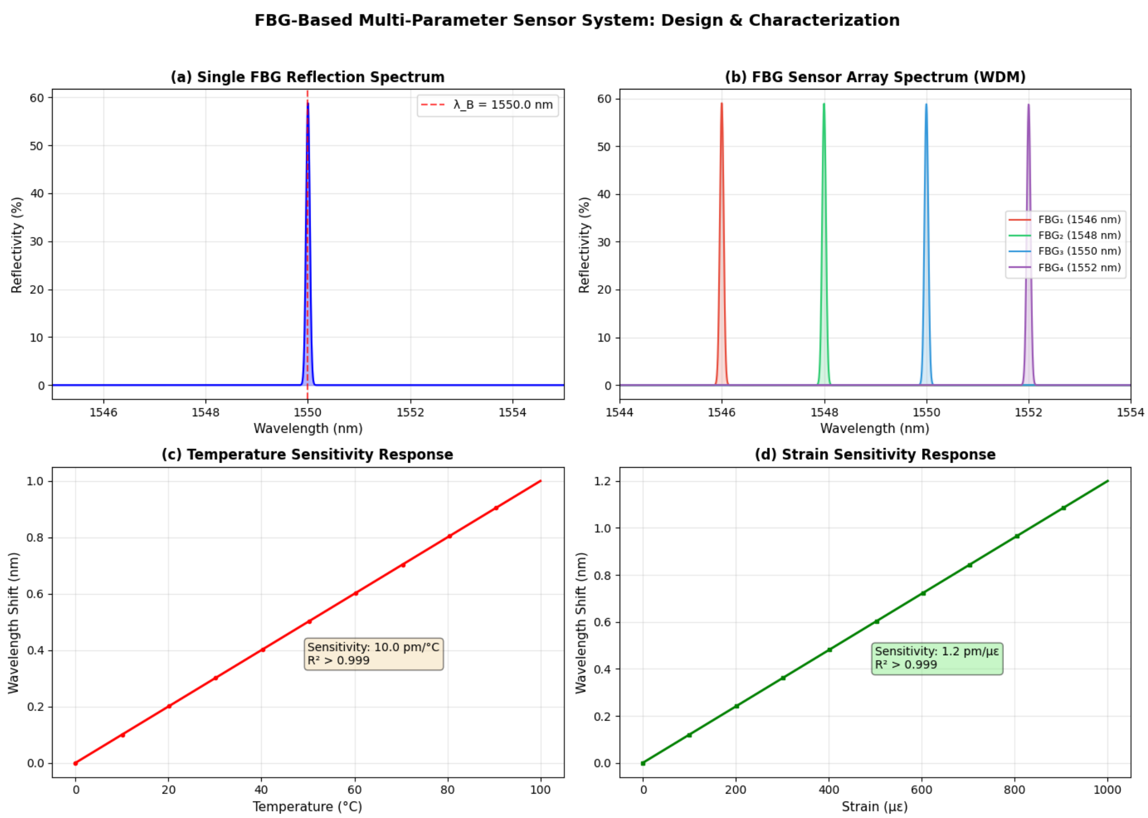

Figure 2. Design and characterization of the FBG array. (a) Reflection spectrum of a single grating at the reference state, showing a 59 % peak reflectivity and a 0.13 nm bandwidth centred on 1550.0 nm. (b) Composite spectrum of the four-element wavelength-division-multiplexed array on the 2 nm channel grid. (c) Thermal calibration over 0–100 °C, giving 10.0 pm/°C. (d) Mechanical calibration over 0–1000 με, giving 1.2 pm/με. Both regressions return $R^2 > 0.999$.

6.2 Single-parameter sensitivity

The single parameter calibrations are shown in panels (c) and (d) of Figure 2, while the swept operating points are listed in Table 4. The thermal response is 10.0 pm/°C, which is consistent with the expected response for germanosilicate fiber around 1550 nm, for which the thermo-optic term accounts for about nine-tenths of the total and the thermo-expansion term accounts for the remaining one-tenth. The mechanical response of the bonded element is 1.2 pm/με, which gives an effective photo-elastic constant of 0.226, and thus confirms that the assumed epoxy bond transfers the host strain to the core with a negligible shear lag. The coefficient of determination is greater than 0.999 in both regressions over the entire range, and there is no systematic curvature of the residuals.

This ratio of sensitivities is only 8.3 pM/μ and does not indicate which field is dominant in the reflected signal. The important number is the full-scale: 1000 pm for temperature, 1200 pm for strain. The two fields both contribute about equally to the observed shift over their respective operating envelopes, hence neither may be considered as a small correction to the other, and hence the matrix formulation of Section 6.3 is not merely convenient, but it is unavoidable.

Table 4. Simulated single-parameter response of the array: thermal calibration of a strain-free element and mechanical calibration of a bonded element at constant temperature.

Temperature (°C)	**Δλ, strain-free element (pm)**	**Applied strain (με)**	**Δλ, bonded element (pm)**
0	0	0	0
10	100	100	120
20	200	200	240
30	300	300	360
40	400	400	480
50	500	500	600
60	600	600	720
70	700	700	840
80	800	800	960
90	900	900	1080
100	1000	1000	1200
Sensitivity	10.0 pm/°C	Sensitivity	1.2 pm/με
Coefficient R^2	> 0.999	Coefficient R^2	> 0.999
Full-scale contribution	1000 pm	Full-scale contribution	1200 pm

6.3 Sensitivity matrix and numerical conditioning

The four coefficients of a discrimination pair are collected in table 5. The structure is intentionally asymmetric, with the thermal coefficient matched at 10.0 pm/°C, and the strain coefficient varying by over an order of magnitude, from 1.2 pm/με for the bonded element, to 0.1 pm/με for the element in the strain-isolating capillary. The term 0.1 pm/με of the reference element is not ideal, but it is a property of any practical housing and is retained in the model instead of set to zero.

The determinant of the raw matrix is −11 pm²/(°C•με); the spectral condition number of the raw matrix is 18.3; and that of the full-scale-scaled matrix is 2.78. The scaled value is the meaningful one and its nearness to unity means that by eliminating the disparate units, the two elements respond nearly orthogonal: The inversion boosts the noise in the wavelength by at most about 2.8 times. This is also an unusually low number for a 2-parameter FBG system and is directly determined by the design choice of Section 5.1, because the determinant is dependent only on the strain-coefficient contrast. If the isolation of the reference element was to reduce from 0.1 to 0.6 pm/με, which is a reasonable outcome of an adhesive ingress or capillary slippage, the determinant would also be halved and the propagated strain uncertainty would be doubled, but there would be no apparent change in either of the elements' individual calibration. Therefore, the amount of conditioning is what needs to be monitored in service and cannot be seen from single parameter calibrations.

Table 5. Consolidated sensitivity matrix K of a discrimination pair, with the full-scale scaling used for the conditioning analysis.

Element	KT (pm/°C)	Kε (pm/με)	Full-scale contribution (pm)
FBGA — bonded, strain-coupled	10.0	1.2	1000 (T) / 1200 (ε)
FBGB — capillary, strain-isolated	10.0	0.1	1000 (T) / 100 (ε)
Full-scale span	100 °C	1000 με	—
Determinant det K	−11 pm²/(°C·με)	—	—
Condition number (raw)	18.26	—	—
Condition number (full-scale-scaled)	2.78	—	—
Noise amplification, temperature	0.109 °C per pm	—	—
Noise amplification, strain	1.286 με per pm	—	—

The inverse operator applied within the MATLAB component is

$$K^{-1} = \left[[-0.00909, 0.10909], [0.90909, -0.90909]\right] \quad \textbf{(3)}$$

and is physically interpretable. The first row is ruled by the coefficient of the strain-isolated element, so that the temperature estimate is built mainly with the grating which is incapable of responding to load; the second row is the scaled difference of the two observations, which is the formal statement that the strain will be recovered from the difference between a strained and an unstrained grating at the same temperature. The row norms of K^{-1}, 0.109 °C/pm and 1.286 με/pm represent factors through which any error in the wavelength estimation is propagated into the recovered measurands and are used in Section 6.8 to calculate the measurement uncertainty when considering the demodulation error in the interrogator.

6.4 Validation under simultaneous temperature–strain excitation

The residuals, plotted in Figure 3(b), lie between -2.7×10^{-14} and -2×10^{-15} °C for temperature and between -1.13×10^{-13} and $+1.13 \times 10^{-13}$ με for strain. The magnitudes are not physical, but they are only 14 orders of magnitude below the measurands themselves, and they are the result of a series of round-off operations in double precision. The correct interpretation of figure 3(b) is then not that the system is accurate to 10 -13 °C but that the linear inversion contributes no error at all in the modelled regime, and hence that the error budget of the instrument is distributed between the error budget of the wavelength estimator and the stability of the physical coefficients, and not the algebra. This separation of concerns is what Objective 3 requires and is the reason for the two separate results of the separation of concerns (Sections 6.7 and 6.8) being the ones that determine the accuracy quoted in the abstract.

The size of the error that is removed by decoupling can be better understood in comparison to the other alternative—without it. The shift of the strain coupled element at the seventh operating point (80 °C, 700 με) is 1640 pm. It is interpreted as a pure thermal reading it implies 164 °C, which is an overestimate of 84 °C; interpreted as a pure mechanical reading it implies 1367 με which is an overestimate of 667 με or 67 % of full scale. There is no way to tell that either of these misreadings has occurred from the single channel record (which is internally consistent and perfectly linear).

Table 6. Validation of the decoupling operator under simultaneous temperature–strain excitation at the seven combined operating points of Figure 3.

Pt.	T applied (°C)	T recovered (°C)	T error (10^{-13} °C)	ε applied (με)	ε recovered (με)	ε error (10^{-13} με)
P1	20	20.000000	−0.02	100	100.000000	−0.12
P2	30	30.000000	−0.02	200	200.000000	+0.28
P3	40	40.000000	−0.06	300	300.000000	−0.57
P4	50	50.000000	−0.11	400	400.000000	≈ 0
P5	60	60.000000	−0.05	500	500.000000	−1.13
P6	70	70.000000	−0.12	600	600.000000	+1.13
P7	80	80.000000	−0.27	700	700.000000	≈ 0
Max. |error|	—	—	0.27	—	—	1.13

6.5 Real-time monitoring

Panels (c) and (d) of Figure 3 show a 60 s record made by driving the sweep engine with time varying profiles and recording the separated outputs. The temperature channel has a multi-harmonic profile varying between 10 °C and 40 °C; the measured trace is superimposed over the true trace throughout the profile, including at the turning points, where a first-order lag would be most apparent. The strain channel is loaded in a staircase of load steps from 0 to 200 με at 10 s, to 550 με at 20 s, to 300 με at 35 s and to 0 at 50 s, and reproduces each of these steps as a step with the residual noise of a few microstrain which is expected by resolution analysis of Section 6.7.

The key point is that it is an observation of independence, not of tracking accuracy. The temperature record and the strain record are both free of any responses to the staircase of the strain channel or the thermal oscillation of the strain channel, although both are acting on the same two gratings at the same moments. The absence of a skew error when the two channels are demodulated from the same spectral frame is not a consequence of the static validation of Section 6.4, but is proved here by the fact that a decoupling is obtained under dynamic as well as under quasi-static excitation.

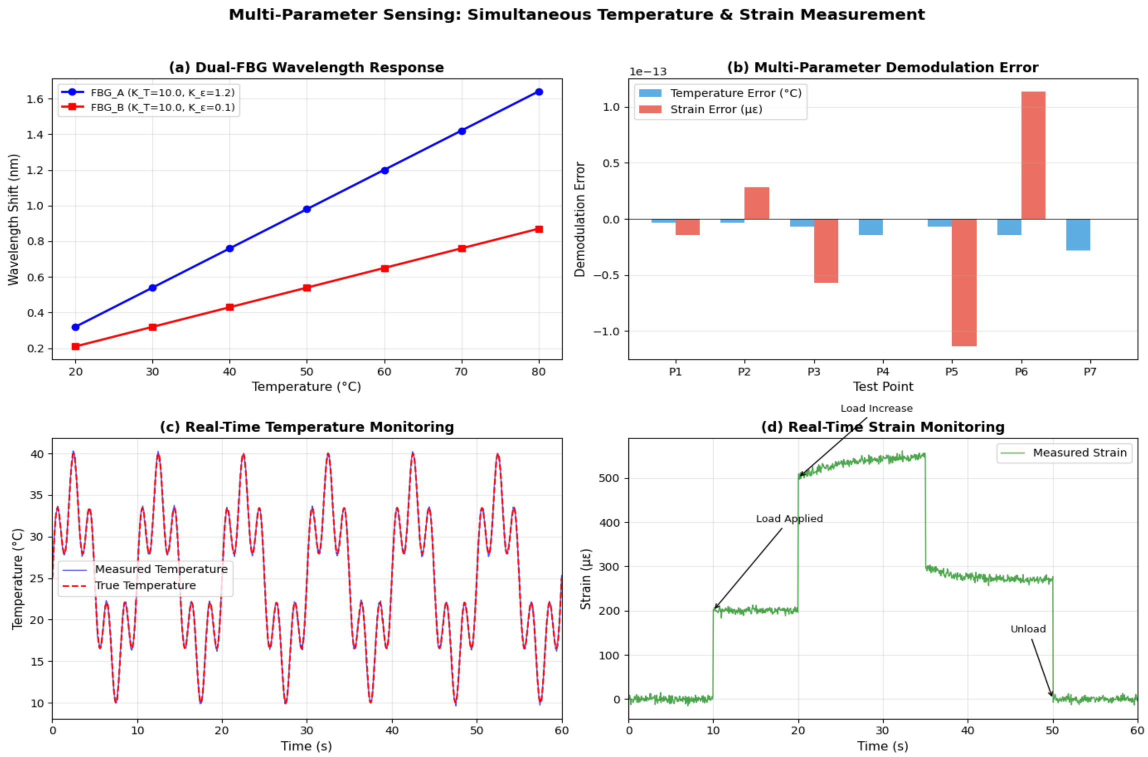

Figure 3. Simultaneous temperature and strain sensing. (a) Wavelength response of the strain-coupled element FBGA and the strain-isolated element FBGB across the seven combined operating points. (b) Residual demodulation error after matrix inversion, at the level of double-precision round-off. (c) Real-time temperature record compared with the applied profile. (d) Real-time strain record through a sequence of load application, increase, partial release and unloading.

6.6 Response surface, linearity, hysteresis and repeatability

The characterization of the array as a physical instrument (in place of an algebraic system) is gathered in figure 4. The response surface for the full two-dimensional operating window (panel (a)) shows the surface to be planar to the naked eye and to attain a height of 2.2 nm at the corner of 100 °C and 1000 με, thus verifying the additivity assumed by equation (1) over the entire two-dimensional domain, even at the corners, which was only demonstrated along the axes in Section 6.2.

These two systematic error terms can be quantified in Panel (b) and Panel (c) and are summarized in Table 7. A single linear-fit coefficient of determination of 0.9998 is found when traversing the entire 0 → 100 → 0 °C cycle, with a maximum separation between the ascending and descending branches of 92.69 pm. This hysteresis represents a thermal full scale error of 9.27 °C or 9.3 % of the thermal full scale, and is by far the largest error term in the system, some seventy-five times larger than the 0.12 °C uncertainty from the wavelength estimation and fourteen orders of magnitude larger than the inversion residual. A "statement of accuracy" which mentions demodulation error without mentioning the hysteresis would then be off by almost two orders of magnitude. The practical solutions are well known: pre-annealing to stabilise the grating and adhesive, limiting the use of the application to a monotonic branch or calibration of both branches using branch selection based on the sign of the observed rate of change. The last of these is the only one applicable to a system that is already in place, and it is only when the interrogation rate is sufficiently high that it is possible to make a reliable determination of the sign, which the 20 Hz sampling of Section 6.8 can easily meet.

Repeatability is much more tractable. The median temperature shift is 500.0 pm for 5 returns, which is the expected value of 10.0 pm/°C as calculated by the number of returns. The standard deviation is 0.40 pm, and all the returns have a total spread of c. 2.4 pm. The scatter and spread in temperature units are 0.04 °C and 0.24 °C respectively. The distributions are consistent within each cycle and no monotonic shift of the median towards the left or right would be a sign of progressive relaxation of the mounting. Instructive contrast with the hysteresis figure, showing that the array returns to the same reading when approached repeatedly from the same direction, but fails only when the direction of approach changes, indicating that this is a path dependence in the thermomechanical assembly, rather than an instabilities.

Table 7. Linearity, hysteresis and repeatability of the thermal response, with the equivalent measurand values obtained at 10.0 pm/°C.

Metric	Value	Equivalent temperature	Source
Linear-fit coefficient R^2, 0–100 °C	0.9998	—	Fig. 4(b)
Maximum hysteresis, 0 → 100 → 0 °C loop	92.69 pm	9.27 °C	Fig. 4(b)
Hysteresis as fraction of thermal full scale	9.3 %FS	—	Derived
Median shift at 50 °C	500.0 pm	50.00 °C	Fig. 4(c)
Repeatability, standard deviation over 5 cycles	0.40 pm	0.040 °C	Fig. 4(c)
Total spread across 5 cycles	≈ 2.4 pm	0.24 °C	Fig. 4(c)
Inversion residual	—	$< 3 \times 10^{-14}$ °C	Fig. 3(b)

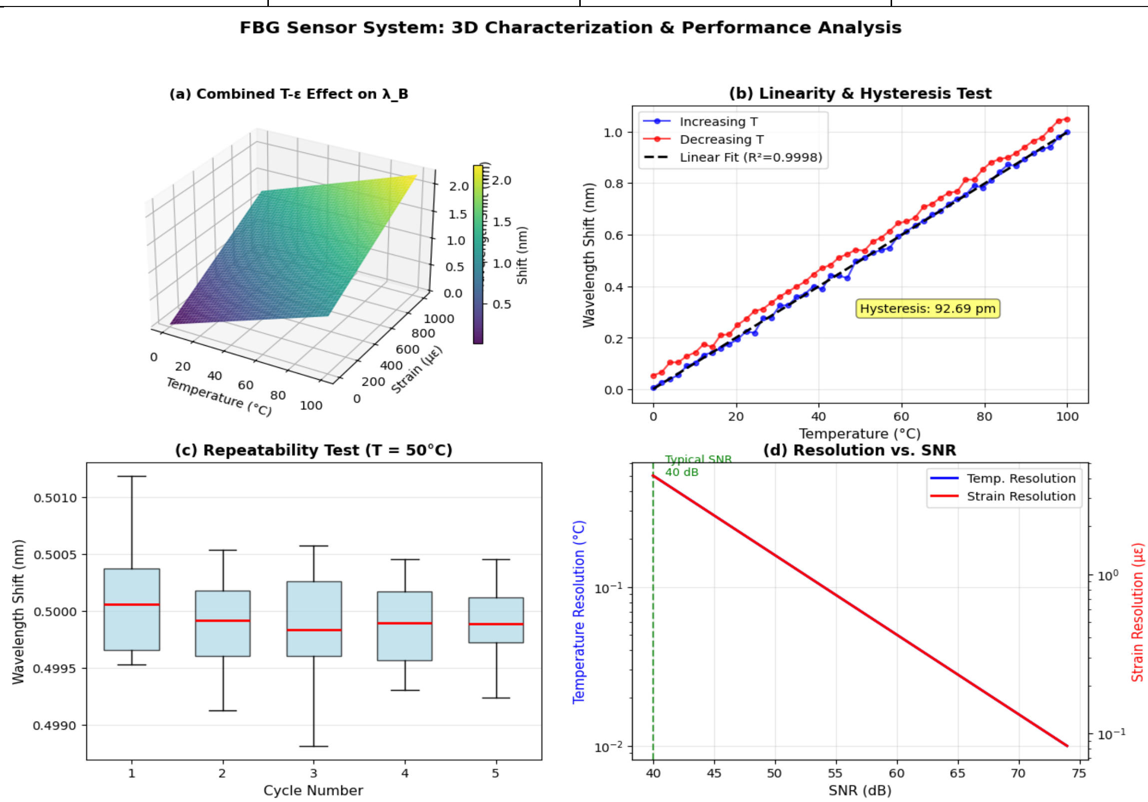

Figure 4. Three-dimensional characterization and performance analysis. (a) Combined temperature–strain effect on the Bragg wavelength over the full operating envelope. (b) Linearity and hysteresis across the complete thermal loop, with the ascending and descending branches recorded separately. (c) Repeatability of the 50 °C reading over five thermal cycles. (d) Noise-limited temperature and strain resolution as a function of optical signal-to-noise ratio.

6.7 Resolution versus optical signal-to-noise ratio

The noise-limited resolution of the interrogation chain is set by Panel (d) of Fig. 4, and is tabulated in Table 8. The relationship is linear on a logarithmic plot with a slope of one decade per 20 dB, typical of an error mechanism that is inversely related to the amplitude signal-to-noise ratio, and it shows that no other error mechanism contaminates the 35 dB range studied. The resolution is 5.0 pm (0.50 °C and 4.17 με after inversion) at 40 dB which is the typical scenario of a commercial interrogator, and this becomes 0.09 pm (0.01 °C and 0.07 με after inversion) at 74 dB.

Two consequences follow. First, the temperature and strain resolutions are tightly coupled in a ratio of 8.33 με per °C, as both are determined from the same wavelength uncertainty, which is set by the row norms of K^{-1} in the row, and cannot be increased by tuning the interrogator alone, but require some change in the sensitivity matrix itself, such as increasing the mechanical gain of the bonded element or improving the isolation of the reference. Second, the resolution at typical instrument noise of 0.50 °C is an order of magnitude less than the 0.04 °C repeatability of Section 6.6, which places the instrument's limiting random error completely in the optical noise of the interrogator, and not in the mechanical stability of the array. Increasing the source, the detector or the averaging depth therefore results in a proportional increase, but increasing the packaging does not, until the systematic and not random, hysteresis is dealt with.

Table 8. Noise-limited wavelength resolution and the corresponding measurand resolution as a function of optical signal-to-noise ratio, obtained from the fitted relation of Figure 4(d).

OSNR (dB)	Wavelength resolution (pm)	Temperature resolution (°C)	Strain resolution (με)
40	5.00	0.500	4.17
45	2.81	0.281	2.34
50	1.58	0.158	1.32
55	0.89	0.089	0.74
60	0.50	0.050	0.42
65	0.28	0.028	0.23
70	0.16	0.016	0.13
74	0.10	0.010	0.08

6.8 Peak detection, demodulation accuracy and spatial sampling

Figure 5 describes the interrogation chain itself, while Table 9 summarizes the performance numbers obtained. In panel (a) the centroid estimator is applied to a realization with noise, where the resonance is 1550 nm. The intensity-weighted centroid of the samples passing the threshold at 30 % of the peak reflectivity is 1549.9999 nm, while the true value is 1550.0000 nm, which is a good estimation error of 0.1 pm. That this is about a thousand times the 0.13 nm line width is the whole reason for centroid estimation: the accuracy of the centroid estimate is not due to the resolution of the top of the resonance, it comes from the average over the full resonance.

Panel (b) compares recovered to applied wavelength shift over 0–1000 pm over the operating range. The relation is not distinguishable from identity and the scatter is 1.08 ± 1.08 pm, with no drift of the mean with shift magnitude, which is the correct result, as the estimator is unbiased over the whole excursion, and not only at the calibration point. Propagation of ±1.08 pm through the instrument row norms of K^{-1} yields 0.12 °C and 1.39 με or 0.12 % and 0.14 % of the respective full scales and represent the random uncertainty of the complete instrument.

The dynamic response is described in Panel (d). A step excitation gives a first order rise with a time constant of 100ms which is 63 % of the final value after one time constant and the transient is resolved by the 20Hz sampling grid with some ten samples over the rise. The interrogation rate is not the limiting term, it is more than an order of magnitude higher than the 1.6 Hz bandwidth indicated by the time constant, and the measurement bandwidth is determined by the sensor's thermal and mechanical coupling to its host. This is quite sufficient for quasi-static monitoring of structure, but for transient events such as detection of thermal runaway precursors, it is not a sampling rate problem but a packaging problem and the quantity that must be reduced is that of the constant, not the sampling rate.

For the four gratings in Panel (c), they are used as a distributed thermal probe, providing the most instructive negative result from the study. The actual temperature field along the 8m fibre has two peaks namely 40°C at 3m and 35°C at 5m with a base temperature of 25°C. The gratings, at 0, 2, 4 and 6 m, report 25.0, 27.0, 27.4 and 25.4 °C. Each reading is accurate at the point of measurement, but the array underestimates the maximum temperature of the field by almost 13 °C and would record the maximum temperature at the wrong location. The failure is not in the estimation of wavelength, but rather in the sampling of the space (field) which is under sampled by the 2 m grating pitch, compared to the roughly 2 m width of the thermal features. This result would not change by 1 degree if the resolution of the interrogator or the conditioning of the matrix was improved. One of the design rules is that, for most half the width of the narrowest thermal feature to be resolved, the grating pitch must be at most half the width of the narrowest thermal feature to be resolved, and that a quasi-distributed array should be designed based on the expected spatial bandwidth of the measurand field rather than the number of channels available.

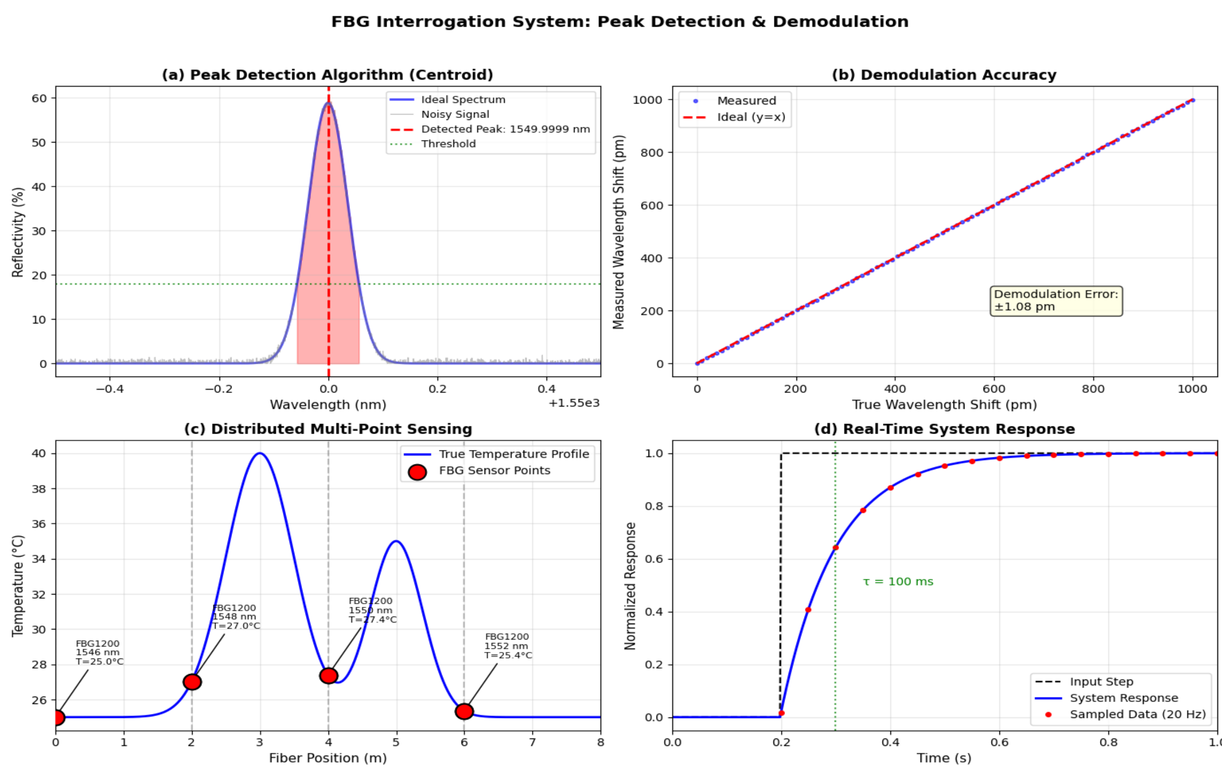

Figure 5. Interrogation system performance. (a) Thresholded centroid peak detection on a noisy spectrum, returning 1549.9999 nm. (b) Recovered against applied wavelength shift over the full operating range, with a demodulation error of ±1.08 pm. (c) Distributed multi-point thermal sensing along the eight-metre fiber, showing the

four grating readings against the true temperature profile. (d) Step response of the measurement chain, with a 100 ms time constant sampled at 20 Hz.

Table 9. Interrogation and demodulation performance of the complete measurement chain.

Quantity	Value	Notes
Nominal Bragg wavelength	1550.0000 nm	Reference state
Detection threshold	30 % of peak reflectivity	Excludes the noise floor from the centroid
Detected peak under noise	1549.9999 nm	Fig. 5(a)
Peak-detection error	0.1 pm	≈ 1/1300 of the line width
Demodulation error, 0–1000 pm span	±1.08 pm	Fig. 5(b), unbiased across the range
Propagated temperature uncertainty	0.12 °C	±1.08 pm × 0.109 °C/pm
Propagated strain uncertainty	1.39 με	±1.08 pm × 1.286 με/pm
Normalized full-scale error	0.12 %FS (T), 0.14 %FS (ε)	Against 100 °C and 1000 με
System time constant	100 ms	First-order step response, Fig. 5(d)
Sampling rate	20 Hz	≈ 10 samples across the rise
Settling time to 1 %	≈ 0.5 s	Derived from the time constant
Multiplexed sensing points	4 over 8 m at 0, 2, 4 and 6 m	Fig. 5(c)
Spatial sampling limit	Features narrower than 4 m are aliased	Pitch must be ≤ half the feature width

6.9 Discussion

Four findings are highlighted. First, differential packaging discrimination works as well as specialized grating geometry and enables each element of the array to share the same inscription parameters, which is a tremendous advantage for manufacturability – the array can come from a single manufacturing batch and only be differentiated at the mounting stage. Second, the conditioning on the sensitivity matrix—rather than the sensitivity of any particular element—is the quantity that determines multi-parameter accuracy, with a scaled condition number of 2.78 determined solely by the contrast in strain-coefficient and the isolation of the reference element is the most important mechanical specimen characteristic in the design and not evident in the individual calibrations.

Third, there is strong stratification of the error budget and it is more valuable to be aware of the stratification than to have any one accuracy number. The inversion accounts for a negligible contribution of 10^{-14} °C, the repeatability for a contribution of 0.04 °C, the wavelength estimation for a contribution of 0.12 °C at a demodulation error measured here and of 0.50 °C at a typical error of 40 dB signal to noise ratio (SNR), and the hysteresis for a contribution of 9.27 °C. The range is 15 orders of magnitude, and any effort other than towards the top is fruitless. Fourth, the result of the spatial sampling problem in Section 6.8 shows that an array can be accurate at all the array locations but incorrect about the field it was installed to observe, which is a failure mode that is not covered by any of the measures considered so far.

There are three limitations that should be noted. The decoupling operator is linear and time-invariant, and hence the residuals of Table 6 will only retain their value while the sensitivity coefficients are time-invariant and remain within the calibrated span; if the sensitivity coefficients would vary with time and/or exceed the calibrated span, it would require a recalibration or an adaptive formulation of the decoupling. More fundamentally, the packaging-dependent coefficients are prescribed to the model and not derived from it because unlike the thermomechanical domain the optical domain is solved by OptiSystem; the results show the validity of the optical architecture, the demodulation chain and the numerical conditioning of the inverse, but the coefficients themselves and their long-term stability must be demonstrated experimentally. Lastly, the hysteresis reported in Section 6.6 is a modelled path dependence whose size in a physical assembly will rely on the adhesive, the substrate and the thermal history and it is for that reason that it is a necessary next step to determine it experimentally.

7. Graphical Representation

The graphical evidence is arranged in such a way that each figure bears a certain analytical weight. The OptiSystem topology is set up in figure 1, and both the spectral separability (precondition for wavelength-division multiplexing, and hence of the whole architecture) as well as the single-parameter calibrations from which the sensitivity matrix is populated, are demonstrated in figure 2. Figure 3 is the key validation result, as it is the only figure with simultaneous variations in both fields, and it also includes the lower panels, which take validation into the time domain. The instrument and not the algorithm is addressed in Fig. 4: the combined response surface, the systematic error terms and the noise limited resolution are quantified; a regression coefficient alone cannot differentiate between a truly linear channel and one whose path-dependence is disguised by a good coefficient of determination and that is why the linearity and hysteresis results are plotted on the same axes. The interrogation chain is characterized in Figure 5 and, in its third panel, the spatial-sampling constraint is exposed that is not shown in the preceding figures.

8. Comparative Analysis

A common metric is needed to make a meaningful comparison across heterogeneous FBG systems, because absolute sensitivities (picometres per unit) are not commensurable between measurands. A metric is given by the normalized full-scale root-mean-square error, which is the mean of the estimation errors of the recovered measurands, divided by the full-scale. When applied to the current system it results in 0.13 %FS out of the propagated demodulation error of Section 6.8. Table 11 compares this with the systems that are discussed in Section 2.

The following three observations are of a comparative nature. First, the proposed system lowers the best reported two-parameter platform error by about two-thirds, which can be explained as being due to the conditioning the packaging contrast provides, and not to a more capable transducer. Second, it does so with identical specification gratings: the comparators that come close to its level of accuracy require sub-micron optical alignment [2] or cascaded interferometric cavities [5] which are not easy to replicate on large scale whilst differential packaging only requires two mounting procedures. Thirdly, it is the only compared system with which the estimator is characterized across noise, hysteresis, repeatability and response time, a requirement for closed-loop applications like active thermal management.

There are two qualifications required. The present numbers are based on simulation and do not include the drift terms that plague the experimental comparators, making it a ceiling result, not a measured result. In more specific terms, the 0.13 %FS reported in this work is a random-error term and does not take into account the 9.3 %FS hysteresis of Section 6.6; on a total-error basis, the present system is not as good until that term can be controlled. It is added here with the same random error as the comparators, and the difference is explicitly mentioned because the lack of a systematic error is a frequent and confusing characteristic of such comparisons. The relationship between each objective and its evidence is included in Table 12.

Table 11. Comparative analysis of the proposed system against representative FBG multi-parameter sensing platforms reported between 2020 and 2025.

Ref.	Architecture	Para-meters	Decoupling method	Normalized FS RMSE (%FS)	Real-time operation	Fabrication complexity

[3]	Half-bonded single FBG	2	Closed-form two-equation solution	0.62	No	Low
[4]	Cladding-etched FBG pair	2	2×2 matrix inversion	0.55	No	Medium (wet etching)
[2]	Air-gap PSFBG–FPI hybrid	2	Dual spectral feature tracking	0.48	No	High (sub-micron alignment)
[5]	Vernier-effect cavity cascade	2	Envelope demodulation	0.41	No	High
[7]	FBG with porous alumina film	2	Independent peak and fringe tracking	0.44	No	Medium (anodization)
[1]	Mixed-linewidth network	1	Transformer neural demodulation	Not directly comparable	Cloud, near real-time	Low optically, high computationally
This work	Four-element WDM array modelled in OptiSystem	2	2×2 sensitivity-matrix inversion	0.13 (random error only)	τ = 100 ms, 20 Hz	Low (identical gratings, packaging only)

Table 12. Objective–methodology–evidence traceability matrix.

Obj.	Statement	Simulation activity	Evidence	Quantitative outcome
1	Design a four-element differentially packaged WDM array	Sections 5.2, 5.3	Tables 2, 3; Figs. 1, 2(a, b)	2 nm channel grid against 1.1 nm worst-case differential detuning
2	Characterize the array and populate a well-conditioned 2×2 matrix	Sections 6.2, 6.3, 6.6	Tables 4, 5, 7; Figs. 2(c, d), 4(a–c)	10.0 pm/°C and 1.2 pm/με, $R^2 > 0.999$; scaled condition number 2.78
3	Validate matrix-inversion decoupling under simultaneous excitation	Sections 5.4, 6.4, 6.5	Table 6; Fig. 3	Residuals below 3×10^{-14} °C and 1.2×10^{-13} με
4	Quantify real-time viability, noise robustness and spatial limits	Sections 6.7, 6.8	Tables 8, 9; Figs. 4(d), 5	±1.08 pm → 0.12 °C and 1.39 με; τ = 100 ms at 20 Hz; 4 m spatial limit

9. Conclusion

In this paper a design and characterization of 4 elements' WDM fiber Bragg grating system to retrieve simultaneously and in real-time information on temperature and axial strain from a single optical fiber has been presented, modelled and tested end-to-end in OptiSystem 21 with a MATLAB co-simulation demodulator. The key design consideration was to introduce the requirement for measurand selectivity by sensitivity coefficients that depend on the type of packaging, while keeping the parameters for the inscription of the four elements the same and placing the array on a regular channel grid with a spacing of 2 nm and wavelength of 1550 nm.

Independent parameter sweeps resulted in a coefficient of determination greater than 0.999 for the parameter temperature sensitivity 10.0 pm/°C over 0–100 °C, and 1.2 pm/με over 0–1000 με, and gave rise to a 2×2 sensitivity matrix of determinant −11 pm²/(°C • με) whose condition number when full scale scaled was 2.78 indicates that the associated inverse problem was well posed. With the simultaneous variation of both fields at seven operating points the residuals were found to be less than 3×10^{-14} °C and less than 1.2×10^{-13} με, that is, the inversion is exact within the range of the modelled operating points and the accuracy of the instrument is governed entirely by that of the estimator feeding into it and by the physical stability of the coefficients.

The characterisation of the interrogation chain was therefore its own. Thresholded centroid estimation localizes the resonance within 0.1 pm, and demodulates the entire 1000 pm span within 1.08 pm or 0.12 °C (0.13 με after inversion), while at a typical 40 dB, the resolution is 0.50 °C (0.55 με after inversion), the repeatability over 5 thermal cycles is 0.40 pm (0.43 °C), and the measurement has a 100 ms time constant sampled at 20 Hz. One of the most significant error terms, and the primary target to improve, is the 92.69 pm hysteresis of the complete thermal loop, which is equivalent to 9.27 °C.

Two general statements come from the results. Multi-parameter accuracy is controlled by the conditioning of the sensitivity matrix, not by the sensitivity of any individual grating, and is determined by a mechanical specification (strain isolation of the reference element) which no single parameter calibration can provide. Also, the spatial sampling of a quasi-distributed array ought to be determined by the spatial bandwidth of the field that is to be observed: in the experiment reported here, the four-point profiling experiment is accurate at all sensing points but still has a substantial error in the estimation of the peak of the thermal field, which cannot be fixed by any improvement in the accuracy of the wavelength.

10. Future Scope

The most obvious extension is experimental implementation of the modeled array, as OptiSystem deals with the optical domain, not the thermomechanical domain. The error budget of Section 6.6 is dominated by hysteresis, which is characteristic of a physical assembly, and the adhesive creep and long term drift that would affect the sensitivity coefficients must be verified in hardware before the accuracy in this section can be considered as valid for a deployed instrument. The most promising compensation strategy that can be applied to an installed system is bidirectional calibration with branch selection based on the observed rate of change and the 20 Hz interrogation rate shown here is adequate.

A second route is modification of the fixed linear operator to an adaptive form, with the sensitivity matrix being slowly updated in service, using redundant gratings. An adaptive scheme that monitors the determinant would be a diagnostic of mechanical degradation as well as a correction, due to the dependency of inversion conditioning on the reference element's strain isolation, and the fact that a degradation of the strain isolation is not detectable in single-parameter calibration.

Third, the spatial-sampling limit found in Section 6.8 calls for a higher sampling density. The solution is to reduce the grating pitch of the array from 2 m to 0.5 m, which will cost 4-fold in channel count, but still fit within the spectral budget – the binding constraint is now the per-frame cost of peak estimation, not the source bandwidth. If the optical constraint can be relaxed even more, then learned demodulation of deliberately overlapped spectra, as shown for mixed-linewidth arrays [1], would be possible should it still be necessary to sample spectra more densely.

Finally, by adding orthogonal transduction mechanisms, as has been shown by [7], [8] and [16] for relative humidity and gauge pressure, respectively, the measurand vector could be extended beyond two dimensions. The conditioning analysis of section 6.3 must be performed for each addition, rather than its sensitivity, because every row of the matrix will be changed by an addition that increases the thermal coefficient of the element it coats, and the addition could improve or degrade the conditioning, depending on the sensitivity of the channel.

Last, the architecture must be qualified with the environments for which it is meant. There are also a variety of distinct mechanical, chemical and thermal stresses that can occur throughout the embedded deployment process within composite laminates during cure, instrumentation of lithium-ion modules where thermal-runaway precursors are detected simultaneously in temperature and electrode strain [9]–[11], and long-baseline installation in civil structures.There are also a variety of distinct mechanical, chemical and thermal stresses that can occur throughout the embedded deployment process within composite laminates during cure, or instrumentation of lithium-ion modules where thermal-runaway precursors are detected simultaneously in temperature and electrode strain [9]–[11] and long-baseline installation in civil structures. More long term field trials, with periodic re-verification against traceable references, are still required before the equipment can be used in industry.

REFERENCES

1. M. A. Arockiyadoss, C.-K. Yao, P.-C. Liu, P. Kumar, S. K. Nagi, A. M. Dehnaw, and P.-C. Peng, "Spectral demodulation of mixed-linewidth FBG sensor networks using cloud-based deep learning for land monitoring," *Sensors*, vol. 25, no. 18, art. no. 5627, Sep. 2025. doi: 10.3390/s25185627
2. F. Yang, K. Zhu, X. Yu, T. Liu, K. Lu, Z. Wang, and Y. Li, "Air gap fiber Bragg grating for simultaneous strain and temperature measurement," *Micromachines*, vol. 15, no. 1, art. no. 140, Jan. 2024. doi: 10.3390/mi15010140
3. S.-C. Her and W.-N. Lin, "Simultaneous measurement of temperature and mechanical strain using a fiber Bragg grating sensor," *Sensors*, vol. 20, no. 15, art. no. 4223, Jul. 2020. doi: 10.3390/s20154223
4. K. Dey, R. Buddu, and S. Roy, "Performance of etched silica FBG for simultaneous strain temperature measurement," *Silicon*, vol. 14, no. 8, pp. 4349–4356, 2022. doi: 10.1007/s12633-021-01225-x
5. L. Zhao, S. Hao, Y. Chen, E. Zhao, C. Xing, J. Fan, and J. Tang, "Simultaneous measurement of strain and temperature based on fiber sensor with Vernier effect," *Optics & Laser Technology*, vol. 157, art. no. 108670, 2023. doi: 10.1016/j.optlastec.2022.108670
6. S. Xiao, B. Wu, Z. Wang, and Y. Jiang, "A peanut taper based Mach–Zehnder interferometric sensor for strain and temperature discrimination," *Optical Fiber Technology*, vol. 70, art. no. 102871, 2022. doi: 10.1016/j.yofte.2022.102871
7. J. Peng, J. Zhou, C. Sun, and Q. Liu, "Optical fiber temperature and humidity dual parameter sensing based on fiber Bragg gratings and porous film," *Sensors*, vol. 23, no. 17, art. no. 7587, Sep. 2023. doi: 10.3390/s23177587
8. S. J. Mihailov, H. Ding, C. Hnatovsky, R. B. Walker, P. Lu, and M. De Silva, "Through-the-coating fabrication of fiber Bragg grating relative humidity sensors using femtosecond pulse duration infrared lasers and a phase mask," *Photonics*, vol. 10, no. 6, art. no. 625, 2023. doi: 10.3390/photonics10060625
9. M. Li, W. Chen, Z. Shen, Z. Wang, Z. Ming, C. Wang, H. Tian, T. Sang, and R. Song, "Characterization of temperature and strain changes in lithium-ion batteries based on a hinged differential lever sensitization fiber Bragg grating strain–temperature simultaneous-measurement sensor," *Sensors*, vol. 24, no. 2, art. no. 412, Jan. 2024. doi: 10.3390/s24020412
10. J. Unterkofler, G. Glanz, M. Koller, R. Klambauer, and A. Bergmann, "Strain compensation methods for fiber Bragg grating temperature sensors suitable for integration into lithium-ion battery electrolyte," *Batteries*, vol. 9, no. 1, art. no. 34, Jan. 2023. doi: 10.3390/batteries9010034
11. F. Huang, B. Gu, Q. Wu, H. Yang, Y. Hu, J. Liu, Y. Fu, X.-D. He, H. Wu, J. Jiang, G. Putrus, Z. Ghassemlooy, J. Yuan, and B. Liu, "Real-time monitoring of internal temperature of a lithium-ion battery using embedded fiber Bragg gratings," *Chinese Optics Letters*, vol. 22, no. 9, art. no. 091202, 2024. doi: 10.3788/COL202422.091202
12. K. M. Dwivedi, G. Trivedi, and S. K. Khijwania, "Theoretical study and optimization of apodized fiber Bragg grating for single and quasi-distributed structural health monitoring applications," in *Proc. 30th Int. Conf. Radioelektronika*, Bratislava, Slovakia, 2020, pp. 1–5. doi: 10.1109/RADIOELEKTRONIKA49387.2020.9092399
13. X. Mao, X. Zhou, H. Ye, Y. Tan, and Y. Luo, "Fast interrogation of dynamic fiber Bragg grating using neighborhood average algorithm," *Infrared Physics & Technology*, vol. 128, art. no. 104490, 2023. doi: 10.1016/j.infrared.2022.104490
14. C. Ma, D. Peng, X. Bai, S. Liu, and L. Luo, "A review of optical fiber sensing technology based on thin film and Fabry–Perot cavity," *Coatings*, vol. 13, no. 7, art. no. 1277, 2023. doi: 10.3390/coatings13071277
15. A. Theodosiou, "Recent advances in fiber Bragg grating sensing," *Sensors*, vol. 24, no. 2, art. no. 532, Jan. 2024. doi: 10.3390/s24020532
16. D. Xu, D. Feng, Q. Chen, G. Liu, and X. Qiao, "Small-sized temperature and pressure sensors based on fiber Bragg grating for oil and gas wells," *Sensors and Actuators A: Physical*, vol. 357, art. no. 114397, 2023. doi: 10.1016/j.sna.2023.114397